

# High-power 95 GHz pulsed electron spin resonance spectrometer

W. Hofbauer, K. A. Earle, C. R. Dunnam, J. K. Moscicki, and J. H. Freed<sup>a)</sup>

*Department of Chemistry and Chemical Biology and National Biomedical Center for Advanced ESR Technology, Cornell University, Ithaca, New York 14853*

(Received 25 November 2003; accepted 26 January 2004; published 22 April 2004)

High-field/high-frequency electron spin resonance (ESR) offers improved sensitivity and resolution compared to ESR at conventional fields and frequencies. However, most high-field/high-frequency ESR spectrometers suffer from limited mm-wave power, thereby requiring long mm-wave pulses. This precludes their use when relaxation times are short, e.g., in fluid samples. Low mm-wave power is also a major factor limiting the achievable spectral coverage and thereby the multiplex advantage of Fourier transform ESR (FTESR) experiments. High-power pulses are needed to perform two-dimensional (2D) FTESR experiments, which can unravel the dynamics of a spin system in great detail, making it an excellent tool for studying spin and molecular dynamics. We report on the design and implementation of a high-power, high-bandwidth, pulsed ESR spectrometer operating at 95 GHz. One of the principal design goals was the ability to investigate dynamic processes in aqueous samples at physiological temperatures with the intent to study biological systems. In initial experiments on aqueous samples at room temperature, we achieved 200 MHz spectral coverage at a sensitivity of  $1.1 \times 10^{10} \sqrt{s}$  spins and a dead time of less than 50 ns. 2D-electron-electron double resonance experiments on aqueous samples are discussed to demonstrate the practical application of such a spectrometer. © 2004 American Institute of Physics. [DOI: 10.1063/1.1710700]

## I. INTRODUCTION

Advances in mm-wave technology have led to the widespread use of high-field/high-frequency electron spin resonance (HFESR) spectrometers in recent years.<sup>1–11</sup> The advantages of HFESR include increased  $g$  factor (Zeeman) resolution and sensitivity.<sup>12,13</sup> In addition, electron spin resonance (ESR) experiments at multiple frequencies greatly help in analyzing spectra that include both field dependent and field independent contributions. A multifrequency approach is also especially useful for dynamic systems, because measurements at different microwave frequencies are sensitive to processes on different time scales.<sup>14,15</sup>

Pulsed ESR techniques, especially in two spectral dimensions, provide greater reliability in analyzing spectra, since they improve spectral resolution to dynamical processes, such as those that occur in complex biosystems.<sup>14–18</sup> Spin echoes enable one to distinguish between the homogeneous broadening, which reports on the spin relaxation and dynamics, and the inhomogeneous broadening, which relates to the local structure in complex materials. The time-domain technique of two-dimensional (2D) electron-electron double resonance (ELDOR) is particularly useful, since it also generates off-diagonal peaks (cross peaks) that directly report on translational and rotational motions in molecular systems.<sup>14–18</sup> 2D-ELDOR is based on Fourier transform techniques, which require the use of short and intense pulses to effectively irradiate the whole ESR spectrum. Given these virtues of time-domain ESR methods, it is desirable to extend Fourier transform ESR (FTESR) to higher frequencies

and magnetic fields. This would permit 2D-ELDOR to be utilized in a multifrequency approach to disentangle processes on different time scales, and it would also benefit from the increased orientational resolution of ESR at high frequencies, which is of considerable value in dynamical studies.<sup>12,14,15,19</sup>

The spectral coverage of an excitation pulse  $\Delta f_{\text{exc}}$  is determined by the duration of the pulse  $t_p$ . But, in order to achieve a specific flip angle of the spins,  $t_p$  depends on the strength of the magnetic field component  $B_1$  of the mm wave in the rotating frame, e.g., for a fast-switched  $\pi/2$  pulse

$$\Delta f_{\text{exc}} \approx K t_p^{-1} = \frac{2K \gamma_e B_1}{\pi} \propto B_1 = \kappa \sqrt{QP}, \quad (1)$$

where  $\gamma_e$  is the gyromagnetic ratio of the spin,  $\kappa$  and  $Q$  are the conversion and quality factors of the resonator, respectively, and  $P$  is the incident mm-wave power;  $K \approx 1.12$  (–3 dB bandwidth) or  $K \approx 1.37$  (–6 dB bandwidth).<sup>20,21</sup>

On the other hand, the –3 dB bandwidth of the resonator  $\Delta f_{\text{res}}$  at a resonant frequency  $f_0$  is

$$\Delta f_{\text{res}} = \frac{f_0}{Q}. \quad (2)$$

The choice of the quality factor  $Q$  is therefore a compromise, which is optimized when  $\Delta f_{\text{exc}} \approx \Delta f_{\text{res}}$ , and thus the achievable bandwidth depends crucially on the available power  $P$ .<sup>21</sup>

Building or obtaining sufficiently powerful, coherent, low-noise micro- and mm-wave sources can be a challenge

<sup>a)</sup>Electronic mail: jhf@ccmr.cornell.edu

at higher frequencies. As a result, existing pulsed HFESR spectrometers<sup>3,6,8,9</sup> have been restricted to output powers in the mW range (with the exception of one early report<sup>5</sup>), corresponding to pulse lengths of tens or hundreds of nanoseconds, and they are able to utilize FTESR methods only for very narrow spectra with long relaxation times. For spectra of wide extent, one typically has had to apply narrow-band field-swept techniques, which have been successful only for long relaxation times, restricting the experiment to low temperatures and organic radicals. Also, this negates the multiplex sensitivity advantage of FTESR and renders correlations between different parts of the spectrum inaccessible, except by traditional double resonance techniques. For work on molecular dynamics of biomolecules in fluid media at physiological temperatures, the homogeneous  $T_2$  relaxation times can be as short as a few ns. This requires a spectrometer with short pulse duration  $t_p$  as well as short dead times  $t_d$  after the pulse. In addition, the short pulse duration  $t_p$  would provide the needed spectral coverage. Thus, just as was the case at microwave frequencies, high mm-wave powers are called for in order to achieve pulses with short enough duration and sufficient spectral coverage. Given the shorter  $T_2$  relaxation times and greater spectral bandwidth at the higher frequencies,<sup>14,19</sup> the challenge becomes, in principle, even more demanding in the mm-wave range.

Below, we describe a HFESR spectrometer developed in our laboratory, featuring 1 kW of pulse power. Special attention has been paid to facilitate large bandwidth Fourier transform experiments with short dead times in aqueous samples, aimed at the investigation of complex systems of biological relevance.

Whereas microwave waveguide techniques were successfully used in the past in low-power spectrometers operating in the 95 GHz range,<sup>3,8,9,11</sup> there is also an example of a successful spectrometer that utilizes quasioptical techniques.<sup>7</sup> Not only did it demonstrate that reflecting, beam-focusing optics could be used very effectively at this frequency, it has the additional virtue that it could also be operated at 180 GHz, where quasioptical techniques become more natural. Our choice of quasioptics for a significant part of our pulsed spectrometer is derived, in part, from this success and from the potential that our high-power pulse spectrometer developments at 95 GHz could be extended to higher frequencies. In addition, there are a number of special features of quasioptical technology that make it very suitable for high-power pulsing which we describe below.

## II. DESIGN AND IMPLEMENTATION

To meet the main goals of short pulse widths and large bandwidth, attention must be paid to several points: (i) A high-power mm-wave source providing sufficiently fast and well-defined pulse shaping has to be used, (ii) path and insertion losses on the way from the source to the sample have to be minimized, and (iii) the conversion factor  $\kappa$  of the resonator has to be maximized while maintaining a low enough quality factor  $Q$  to accommodate the bandwidth of narrow pulses.

The key aspects of the spectrometer described here are:

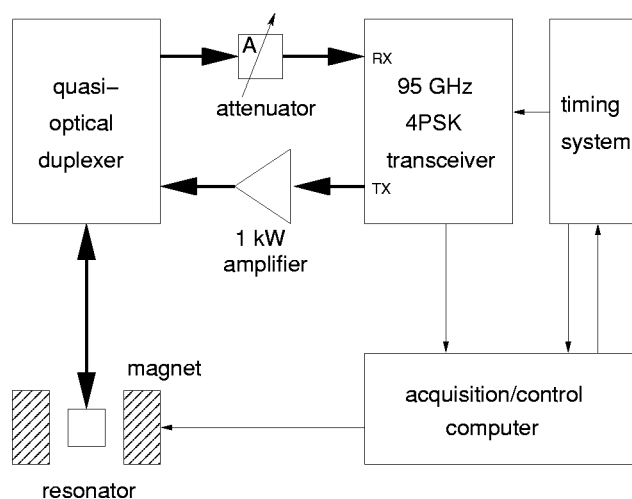


FIG. 1. Spectrometer block diagram. The low-power (90 mW) transmitter–receiver is augmented with a 1 kW mm-wave amplifier. Transmit and receive signal paths are duplexed in a quasioptical setup. Process control and data acquisition tasks are performed by a computer.

The use of a specialized mm-wave amplifier tube to achieve sufficient power output; relying on quasioptical techniques in the high-power stages to reduce power losses and maintain low dispersion; and a compact Fabry–Pérot resonator with a novel variable coupling method that operates in the induction mode to isolate the detection arm from the incident high-power pulses. A block diagram of the spectrometer is shown in Fig. 1. The transceiver utilizes more conventional waveguide technology whereas the duplexer (high-power bridge) and the resonator are based on quasioptics.

### A. Transceiver

A custom-specification, commercial 95 GHz transceiver (ELVA-1, St. Petersburg, Russia) is used for the generation and detection of the mm-wave signals (Fig. 2). The transceiver has separate WR-10 waveguide ports for transmitted and received signals which simplifies the insertion of external components into the signal path.

The 95 GHz signal is derived from a 7.168 GHz dielectric resonator oscillator. Alternatively, an external frequency source can be used, which allows limited ( $\pm 130$  MHz) frequency sweeps. The signal is translated to 7.308 GHz using a 140 MHz crystal oscillator as a reference. An IMPATT frequency multiplier ( $\times 13$ ) is used to create the 95 GHz signal, and further IMPATT diode stages are used to achieve an output power of 90 mW.

A manually adjustable phase shifter is fitted just before the multiplier stage whereas electronically switchable  $90^\circ$  and  $180^\circ$  phase shifters operate at 95 GHz. On–off amplitude shift keying (pulse forming) is also performed at 95 GHz, with multiple *p-i-n* diode switches providing the necessary isolation. For continuous wave transmission, these *p-i-n* diode switches can be biased continuously in the low-attenuation regime. A further *p-i-n* diode acts as a continuously variable output attenuator.

The receiver is a dual conversion design. The 95 GHz input signal is downconverted to 1.82 GHz ( $13 \times 140$  MHz) where amplification takes place. The I.F. signal is finally

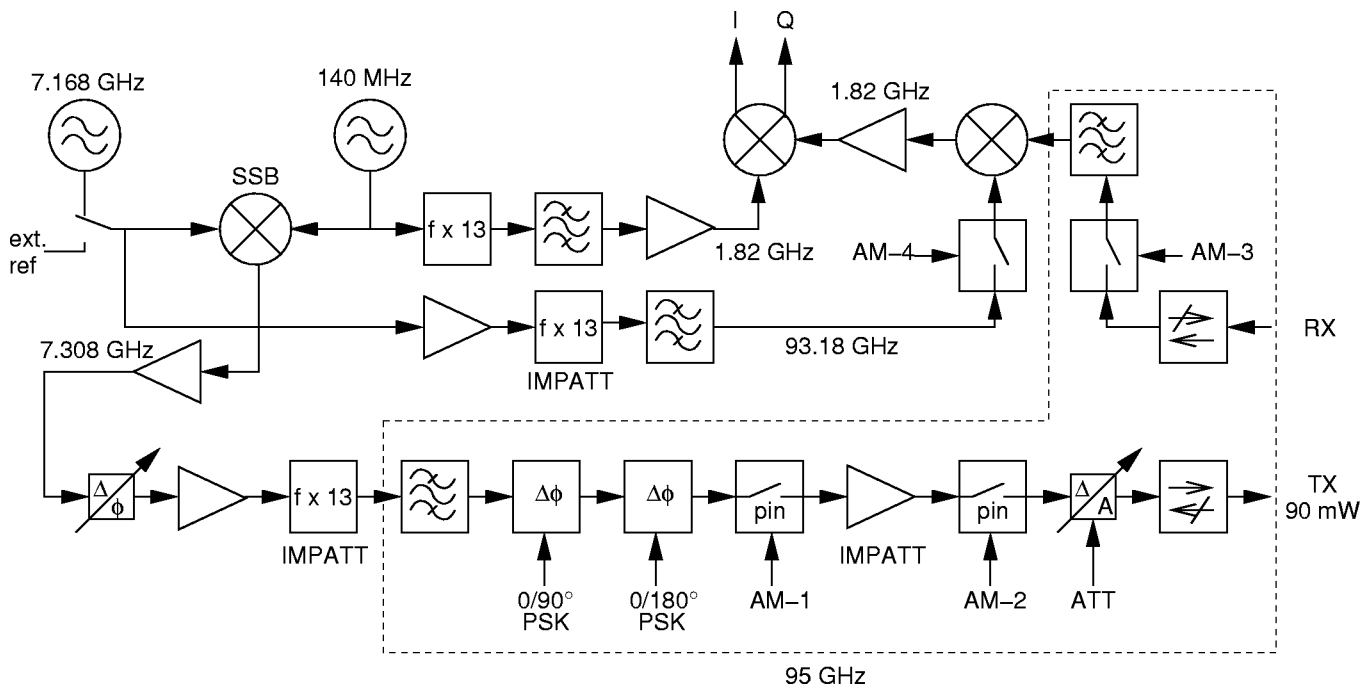


FIG. 2. Block diagram of the ELVA-1 95 GHz transceiver. Pulse shaping and phase shift keying (PSK) are performed at 95 GHz. The receiver uses an intermediate frequency of 1.82 GHz. Separate WR-10 waveguide ports for the transmitter and receiver sections allow for easy insertion of external amplifiers.

converted to baseband in a quadrature mixer. To maintain phase coherence with the transmitted signal, the reference signals for the mixers are derived from the 7.168 GHz and 140 MHz master oscillators using frequency multipliers.

A *p-i-n* diode switch can be used to protect the receiver input from overload during transmission. Saturation of the intermediate frequency (I.F.) amplifier can be further reduced by attenuating the reference signal, and thereby the gain, of the first mixer by 30 dB. A summary of the transceiver characteristics is given in Table I.

## B. Extended interaction amplifier

An extended interaction klystron (EIK, Communications and Power Industries, Georgetown, ON, Canada, type VKB2469T) is used to amplify the mm-wave pulses to  $\approx 1$  kW. The electron tube uses electron velocity modulation similar to a klystron, but has multiple resonators to achieve a larger bandwidth ( $>500$  MHz).<sup>22</sup> The tube exhibits small-

signal amplification of  $\approx 57$  dB at an operating voltage of 16 kV. In our application, the tube is operated in the saturated regime, with a power conversion efficiency of 12% and a maximum duty cycle of 1%.

The EIK tube is controlled by a modulator system of our own design, which enables and disables the amplifying function. To prevent dark noise pickup by the receiver during the detection period at small dead times, the electron beam has to be shut off within a few ns after the last pulse. This switching action requires potential changes of several kV at the annular aperture electrode of the tube, resulting in high peak current transients ( $di/dt = 40$  A/ns) and the potential for severe radio-frequency (rf) noise, which would interfere with the detection of ESR signals. To minimize these problems, the modulator electronics are contained in a rf tight enclosure directly attached to the EIK tube. The enclosure is filled with SF<sub>6</sub> to prevent arcing, and various sensors are used to shut down the modulator in the case of arcing or other dangerous conditions, in order to protect the tube.

If desired, output power can be reduced by a variable waveguide attenuator (Dorado International, Seattle, WA, USA) immediately following the EIK. As opposed to reducing the input power, this approach also reduces the dark noise of the EIK and provides limited protection against a high standing wave ratio at the output of the amplifier unit. A  $-30$  dB directional coupler (Aerowave, Medford, MA, USA) and a diode detector (Hughes, now Millitech, Northampton, MA, USA) are used to monitor such reflected signals.

For low-power experiments, the EIK can be bypassed using a WR-10 waveguide switch (Quinstar Technology, Torrance, CA, USA, model OWM-W00000) (Fig. 3).

TABLE I. ELVA-1 95 GHz transceiver specifications.

Parameter	Unit	Value
Nominal operating frequency	GHz	95.0
Maximum power output	mW	92
Spectral linewidth	kHz	$<1$
Frequency drift	kHz/h	$<100$
Amplitude keying ratio	dB	95
Amplitude rise/fall time	ns	1
Phase shifter accuracy	degrees	$<5$
Phase settling time	ns	5
Receiver gain	dB	37.5
Receiver bandwidth	MHz	700
Receiver noise figure	dB	10.5

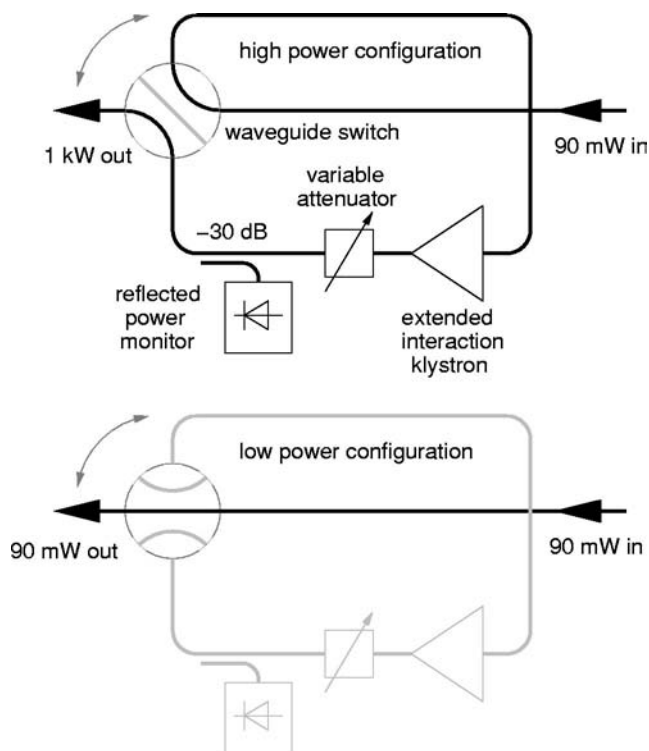


FIG. 3. 1 kW amplifier section using an extended interaction klystron. A diode detector is used for monitoring reflected power. The amplifier can be bypassed for low-power experiments.

### C. Duplexer

Transmitted and received mm-wave signals are combined into a single path using a polarization-coded, quasi-optical, duplexer (Fig. 4). Polarization coding provides for maximum isolation between excitation and detection signals, simplifies the construction of the duplexer, and, in combination with the use of free-space quasi-optical Gaussian beams, results in minimal power losses. These features are successfully achieved with a spectrometer detecting the induction signal of the sample.

A corrugated horn with integral mode transition (Thomas Keating, Billingshurst, West Sussex, UK) converts the WR-10 TE<sub>10</sub> waveguide mode to a hybrid HE<sub>11</sub> mode that is well matched (0.18 dB insertion loss) to a free-space fundamental Gaussian beam mode,<sup>23</sup> with the beam waist (diameter  $w_0 = 14.13$  mm) close to the aperture of the horn. A home-built free-standing wire grid polarizer<sup>24</sup> and a 45° Faraday rotator (Thomas Keating, UK) isolate the transmitter from reflected power and reduce standing waves. The wire grid is used in reflective mode to serve as a planar polarizing mirror. This dual function helps to achieve a compact design. An ellipsoidal off-axis mirror ( $f = 83.24$  mm, machined under computer numerical control in house from aluminum) refocuses the beam. The convergent beam is then reflected by another wire grid which facilitates the duplexing function of the unit. The beam waist is imaged at unity gain to a port which is coupled to the corrugated waveguide used in the probehead.

The cross-polarized induction signal path is identical to the excitation signal path, except that the duplexer and receive path isolator wire grids are used in transmission mode.

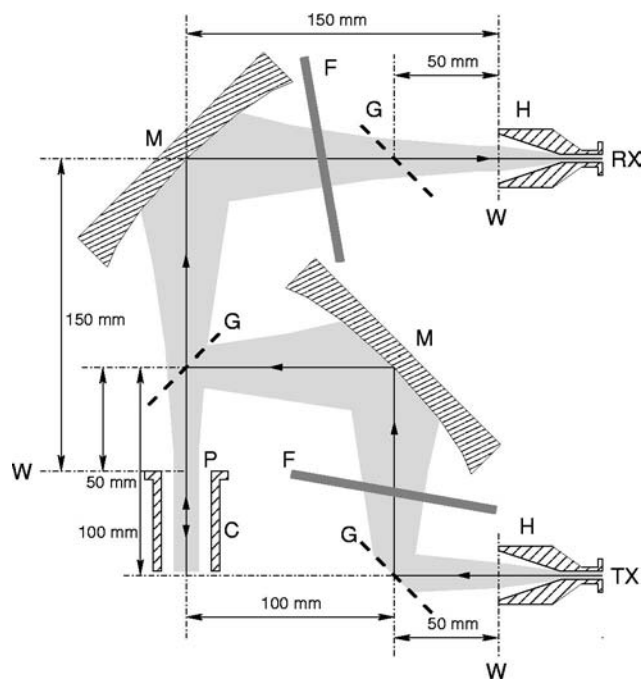


FIG. 4. Quasi-optical polarization coded duplexer unit. H: WR-10/corrugated horn transition; M: Elliptical mirrors ( $f = 83.24$  mm); G: Polarizing wire grids; F: 45° Faraday rotators; P: Waveguide port; C: Corrugated waveguide (to resonator); TX/RX: Transmit/receive WR-10 waveguide flange; W: Location of Gaussian beam waist ( $w_0 = 14.13$  mm). Unused duplexer ports are terminated with absorber pads (not shown) to reduce scattered radiation, standing waves, and coupling to higher-order Gaussian beam modes.

The unused ports are terminated in beam dumps to reduce standing waves and scattering.

It should be noted that, in contrast to some other quasi-optical spectrometers,<sup>4,7</sup> the duplexer is not based on a frequency independent Gaussian telescope. Compared to the center operating frequency of 95 GHz, even a bandwidth of several hundred MHz is narrow enough to eliminate the need for a broadband design.

The small number of components minimizes losses and reduces the potential for undesired reflections. Such reflections would give rise to parasitic resonances, causing non-uniform frequency response and lengthening the dead time  $t_d$  by ringing. Furthermore, the compactness of the unit ( $\approx 200 \times 300 \times 100$  mm<sup>3</sup>) lowers the  $Q$  of such resonances, ameliorating their negative effects.

### D. Probehead

The ESR probehead is designed to be inserted into a vertically aligned magnet bore. A 900 mm long,  $\approx 20$  mm inner diameter (i.d.) circular corrugated waveguide (Thomas Keating, UK) is used to transfer the mm-wave energy between the quasi-optical duplexer and the resonator. The corrugated waveguide preferentially allows propagation of two orthogonally polarized HE<sub>11</sub> modes (used for the excitation and induction signal) with a beam profile that closely matches the Gaussian beam waist at the duplexer port.<sup>23</sup>

The corrugated waveguide is preferred over a conventional waveguide, because the surface conductivity of smooth-wall waveguide decreases with increasing frequency,

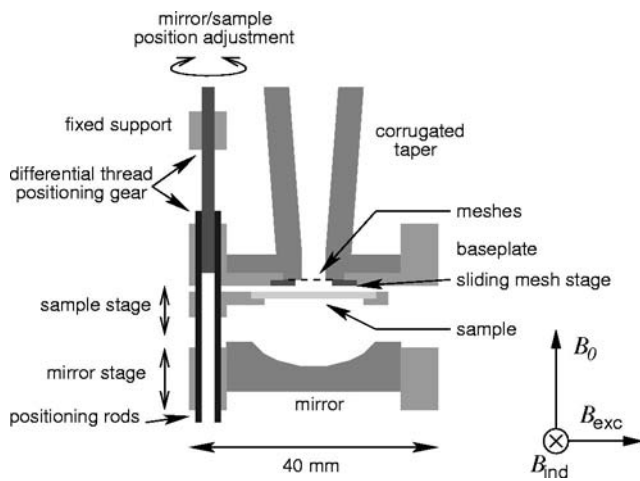


FIG. 5. Simplified cross section of the Fabry-Pérot resonator. The static magnetic field  $B_0$  is parallel to the optical axis, while the excitation ( $B_{\text{exc}}$ ) and induction ( $B_{\text{ind}}$ ) fields are in the plane of the sample.

leading to disproportionate dissipation by wall currents. The corrugations transform the wave impedance of the waveguide wall from small and resistive to large and reactive, thereby suppressing wall currents and their attendant ohmic losses. Thus, we estimate a loss of no more than 1–2 dB from the mm-wave source to the resonator, compared to about a 13 dB loss for a system utilizing a WR-10 waveguide reported elsewhere.<sup>6</sup> While the use of an overmoded smooth-wall waveguide can reduce the transmission losses to about 3 dB,<sup>8</sup> it is not quite as effective as a corrugated waveguide, nor does it preserve the polarization purity of the beam.<sup>25</sup> The latter is essential for operating the spectrometer in the induction mode.

### E. Resonator

A Fabry-Pérot resonator geometry was chosen as its  $\text{TEM}_{00m}$  modes closely match the waveguide  $\text{HE}_{11}$  mode, allowing for efficient coupling (Fig. 5). This eliminates the need for mode conversion devices which often create regions of increased electric-field strength and are, therefore, prone to arcing under short intense mm-wave pulses. Also, a Fabry-Pérot resonator inherently provides orthogonally polarized degenerate modes, which makes it easy to implement an induction-mode spectrometer. Finally, the openness of the resonator structure reduces eddy currents in continuous wave (cw) experiments using  $B_0$  field modulation or in field-stepped experiments and provides easy access to the sample, e.g., for light excitation.

The magnetic and electric-field components of the standing 95 GHz wave in the resonator are oriented perpendicular to the optical axis, while the static magnetic field  $B_0$  is parallel to the axis. Two orthogonally polarized  $\text{TEM}_{00m}$  modes are utilized for the excitation mm-wave field and the induction signal, respectively.

A corrugated waveguide taper is used to focus the mm-wave power and increase the magnetic field strength  $B_1$ . The resulting waist diameter of the emitted pseudo-Gaussian beam is  $\omega_0 = 4.45$  mm. As a result of the narrow aperture which is only slightly larger than one wavelength ( $\lambda = 3.2$

mm), the beam spreads considerably and the phase fronts exhibit significant curvature as the distance from the aperture increases. This curvature must be matched by the mirrors that define the resonator for efficient coupling between the waveguide and resonator modes. A planar semitransparent mirror, discussed in detail below, is positioned at the location of the beam waist, which is very close (0.2 mm) to the aperture of the corrugated taper. The second mirror is spherically concave and was milled from copper using a  $d = 19$  mm ball cutter.

The distance between the mirrors is about 7 mm (corresponding to a mode number of  $m \approx 5$ ) and can be changed via a differential lead screw reduction drive mechanism to adjust the resonance frequency. The control rods used to actuate the drive therefore perform a rotary motion, and the resonator adjustment is less susceptible to instabilities caused by thermal expansion or vibration of the control rods.

The chosen mirror separation is a compromise. The electromagnetic field energy is distributed over the volume  $V$  of the resonator, and the magnetic field strength scales with the conversion factor  $\kappa$  introduced in Eq. (1) as<sup>21</sup>

$$B_1 \propto \kappa \frac{1}{\sqrt{V}}. \quad (3)$$

A smaller mirror separation therefore leads to higher  $B_1$  and increased excitation bandwidth [Eq. (1)]; alternatively, if  $B_1$  is already sufficiently strong, a lower  $Q$  can be afforded, resulting in increased resonator bandwidth [Eq. (2)] as needed to optimize performance. A larger separation, however, makes it easier to accommodate an adjustable sample stage. We estimate a loaded  $Q$  of 300 for our resonator containing an aqueous sample.

Careful analysis<sup>26,27</sup> shows that our resonator design leads to a well-defined Gaussian beam, and we compute<sup>3</sup> an effective resonator volume of  $V \approx 27$  mm<sup>3</sup>. A fundamental  $\text{TE}_{011}$  cavity resonator<sup>6</sup> at 95 GHz would have an effective volume of  $V \approx 6$  mm<sup>3</sup>. Thus, from Eq. (3), the Fabry-Pérot resonator achieves about one-half the magnetic field  $B_1$  of a  $\text{TE}_{011}$  cavity, all other things being equal. We note, however, that it would be more difficult to operate such a cavity in the induction mode. The other advantages of the Fabry-Pérot resonator have been noted at the beginning of this section.

The required  $\pi/2$  pulse length should scale depending on the mm-wave power  $P$ , the loaded  $Q$ , and the effective resonator volume  $V$  according to Eqs. (1) and (3). We find this proportionality to be consistent to within a factor of 2 when comparing the performance of our spectrometer with another report.<sup>8</sup> Given our experimental uncertainties in establishing values for  $Q$ ,  $P$ , and  $V$ , we regard the agreement as satisfactory.

The resonator support structures were machined from G-10 glass fiber laminate. Brass screws and rods are used for the adjustment mechanism.

#### 1. Sample geometry

The sample is inserted between the mirrors, close to the beam waist. In this region, the  $B_1$  field strength is maximum and the phase fronts have negligible curvature, allowing the use of planar samples. A second differential lead screw



FIG. 6. Variable coupling arrangement. By shifting stacked inductive meshes relative to each other, the effective hole size and the reflectivity can be adjusted. The square shape of the holes is maintained and ensures the existence of orthogonally polarized degenerate resonator modes used for excitation and detection.

mechanism allows positioning the sample in a node of the electric field. This adjustment is critical to minimize dielectric losses, particularly with aqueous samples.

Small solid samples are mounted on a thin ( $\approx 75 \mu\text{m}$ ) Mylar sheet using an inert adhesive, e.g., silicone grease. Liquid samples are enclosed in a sandwich configuration in order to avoid evaporation and prevent rapid paramagnetic relaxation via oxygen contamination. For nonpolar solvents, we use sandwiches made from Mylar film; for aqueous samples, the liquid is contained between microscope glass cover slips. Aqueous samples have a typical thickness of  $\approx 25 \mu\text{m}$  and an effective sample volume of  $\approx 500 \text{ nl}$ . Non-polar solvents allow for considerably thicker samples if desired, without unduly damping the resonator mode.

## 2. Resonator coupling

Special attention needs to be paid to the method for coupling the mm-wave field to the Fabry–Pérot resonator. Traditional coupling schemes used for closed resonators, e.g., variable iris coupling, cannot be used because of excessive mode conversion caused by diffraction. Matching techniques based on inline or “stub” impedance transformation networks external to the resonator are commonly used in cw spectrometers. Such resonant networks effectively add to the resonator volume  $V$ , reducing the conversion factor  $\kappa$  and, thereby, the field strength,  $B_1$  [Eq. (3)]. If a desired field strength,  $B_1$ , is to be maintained at the sample, the compound  $Q$  of the arrangement has to be increased, reducing the bandwidth. This limits the usefulness of external coupling networks for high-bandwidth pulsed experiments. Internal matching networks as used in a shunt resonator<sup>28</sup> present similar problems. A solution to this challenge is to use an irislike coupling technique while suppressing diffractive mode conversion. This is achieved by varying the reflectivity of the semitransparent mm-wave mirror through which the mm-wave field is coupled into the resonator.

Initial attempts using a set of interchangeable inductive meshes with different wire spacing<sup>29,30</sup> as semitransparent mm-wave mirrors quickly allowed us to identify the need for continuously adjustable reflectivity. We created, therefore, a composite mesh arrangement as shown in Fig. 6. By shifting the position of two stacked inductive meshes, the effective hole size of the arrangement can be changed. This is similar to the iris coupling techniques, except that diffraction side-lobes are suppressed by the repetition of the iris on an appropriately chosen 2D lattice grid. Since, in an induction

mode spectrometer, the resonator needs to support two degenerate modes with orthogonal polarization, it is essential to maintain the symmetry of the coupling holes. This is achieved by choosing square holes in the individual meshes and carefully aligning the translation axis for adjusting the hole size, so as to maintain the square aperture shape.

To first order, the reflection properties of this symmetric mesh pattern are isotropic. In practice, we have found that the mesh performance depends slightly on the orientation with respect to the polarization of the incident mm-wave. While this effect can often be neglected, it can help in fine tuning resonator performance and minimizing crosstalk between the excitation and detection mode.

The free-standing meshes used in our spectrometer were manufactured from  $25.4 \mu\text{m}$  thick copper foil using a photolithographic process and wet chemical etching. The total thickness of the coupling mesh stack is therefore slightly above  $50 \mu\text{m}$ , and, at a wavelength of  $\lambda \approx 3.2 \text{ mm}$ , can be neglected. The surface roughness introduced by the staggering of the two meshes is about  $\lambda/125$ , significantly better than specifications for precision laser optics ( $\lambda/20$ ). The lattice constant chosen is  $g = 1.78 \text{ mm} \approx 0.56\lambda$ , which is small enough to suppress all but the principal diffraction order. The width of the “wires” is 45% of the lattice constant. The size of the square holes in the composite mesh arrangement can therefore be varied from 10% to 55% of  $g$  ( $0.18 \text{ mm}$  to  $0.98 \text{ mm}$ ). This allows us to achieve critical coupling over the range from an empty resonator to  $>25 \mu\text{m}$  thick aqueous samples at room temperature.

## 3. Tuning procedure

Tuning of the resonator is conveniently performed by observing the reflection coefficient of the resonator. During high-power pulses, reflected power leakage through the isolator in the quasioptical duplexer is sufficient to monitor the reflected power on the diode detector shown in Fig. 3.

The position of the mirror, the sample, and the setting of the coupling mesh are adjusted iteratively to minimize the reflected signal. The resonance frequency is greatly affected by the sample position. Dielectric losses in the sample tend to reduce the resonant frequency, which would be compensated for by decreasing the mirror distance. Reversing this argument, the position of minimal dielectric losses can be typically found by maximizing the mirror distance while maintaining resonance using the sample position adjustment. Adjusting the coupling mesh affects both the magnitude and the phase of the reflection, and both the spherical mirror and the sample have to be moved accordingly to compensate for this phase shift and maintain resonance.

In the low-power configuration, the reflected power monitor is bypassed (Fig. 3), and reflections cannot be observed in the same way. Instead, the received signal can be monitored. Due to imperfections of the resonator and asymmetries of the sample, a small amount of the reflected signal is cross polarized and can be observed using the receiver. The phase coherence of the receiver enables us to monitor the phase change of the received signal while adjusting the mirror spacing, indicating resonance. Furthermore, in low-power operation, it is usually desired to monitor the induc-

tion signal during mm-wave excitation. The resonator coupling is, therefore, typically adjusted to minimize crosstalk between the two modes. By rapidly switching the phase of the transmitted mm-wave, the crosstalk signal shows up as an ac component on the receiver output and is easily distinguished from receiver dc offsets.

## F. Magnet

The vertically aligned magnetic field,  $B_0$ , is generated by a superconducting 6 T solid-state nuclear magnetic resonance (NMR) magnet (Oxford Magnet Technology, Witney, Oxfordshire, UK, custom model). The main coil is equipped with a superconducting switch and can be left in persistent field mode without consuming power. At 95 GHz, the field for  $g=2$  transitions is  $B_0 \approx 3.4$  T. A coaxial superconducting sweep coil allows one to sweep the magnetic field over a range from  $-0.05$ – $+0.05$  T around the center field. The sweep coil does not have a superconducting switch, which reduces hysteresis effects and makes it easier to achieve linear field sweeps and stable stationary fields. An IEEE-488 controlled power supply (Hewlett Packard 6032A) is used to drive the main coil. The sweep coil current is provided by a custom supply (Oxford, UK) controlled by an analog signal.

Access to the sample space is possible both from the top and the bottom through a warm bore (i.d.=54 mm). In the current implementation, the transceiver/duplexer unit is mounted above the magnet, and the probehead is inserted from the top. The center of the magnetic field is  $\approx 0.75$  m below the top flange of the bore.

## G. Control/acquisition

### 1. Computer control

An industrial personal computer (Kontron America, San Diego, CA, USA) running Debian GNU/Linux controls the spectrometer and serves as a host to the digitizing averagers described below. External devices are controlled via an IEEE-488 interface and a parallel port.

The control and acquisition software is written in Python, an interactive, high-level, object-oriented, language.<sup>31</sup> Python provides bindings to a multitude of numerical and visualization packages, such as LAPACK,<sup>32</sup> FFTPACK,<sup>33</sup> and GNUPLOT.<sup>34</sup> Control over the spectrometer hardware, which relies in part on external driver libraries, is encapsulated in Python modules as well. Modules, e.g., implementing a specific type of experiment, can be written or updated independently and dynamically loaded without having to restart the acquisition program. These “building blocks” allow one to create experiments and manipulate data with ease in an intuitive and interactive fashion without losing the flexibility of a full-featured programming language. So far, we have not found the performance penalty associated with interpreted languages (as opposed to an optimized compiled program) to be problematic.

Phase cycled multidimensional experiments create significant amounts of data. Some data reduction, e.g., extraction of a certain coherence pathway, has traditionally been performed during acquisition to reduce memory requirements, even with modern spectrometers using workstation-

class computers.<sup>9</sup> If several coherence pathways are desired, the same experiment had to be performed multiple times with such a system.

With contemporary computers, it is in many cases practical to store the complete raw data set. This allows the user to defer the extraction of multiple, arbitrary, coherence pathways until after the experiment. Even if only a single signal component is desired, access to signals arising from the suppressed coherence pathways prove useful in the identification and assessment of instrumental or other experimental artifacts. Experimental data is stored along with all experimental parameters and supplementary information, e.g., comments or detailed sample descriptions, in a single data object. This eases housekeeping tasks compared to other systems that store experimental data and parameters in separate files. Arbitrary extensions can be added to these data objects without breaking existing software or having to extend the file format used for external storage, which has proved useful during the ongoing evolution of the acquisition software.

A special module supports the automatic creation of fully phase cycled experiments ( $4^n$  steps for a  $n$  pulse experiment using  $90^\circ$  phase increments), providing maximum separation of signal components and suppression of artifacts. Signal components may be automatically extracted from the resulting raw data, with the user only specifying the desired coherence pathways. This feature helps one avoid the error-prone tasks of designing and entering lengthy phase tables and facilitates the use of long phase cycles.

### 2. Timing system

The timing subsystem creates control signals for various functions of the spectrometer that include: Generation of mm-wave pulses with defined delays and widths, selection of a desired phase for each mm-wave pulse, turning on and off the high-power amplifier tube, protecting the receiver from overload or damage while the transmitter is active, and providing a trigger signal for the acquisition of the ESR signal. The system currently used (Fig. 7) supports sequences of up to three mm-wave pulses, but will be updated to support more complex sequences (see Sec. IV).

A master delay generator (Stanford Research Systems, Sunnyvale, CA, model DG535) provides four delay channels and a built-in rate/trigger generator. For standard experiments, the rate/trigger generator is used to start the pulse sequence at a specified repetition rate. It is also possible to trigger the delay generator in response to external events, e.g., in response to the firing of a pulsed laser for the study of photogenerated radical species. One delay channel is used to start the data acquisition. The remaining delay channels mark the start of the three possible mm-wave pulses. The master delay generator is programmed by the acquisition computer via an IEEE-488 interface.

The mm-wave pulse markers generated by the master delay unit are routed through separate single-channel delay generators (Berkeley Nucleonics, San Rafael, CA, model 7030A). These secondary delay generators generate pulses of adjustable duration at the delay times marked by the master delay generator. The pulses are then routed to a pulse distribution unit (PDU). The PDU can enable/disable (gate) the

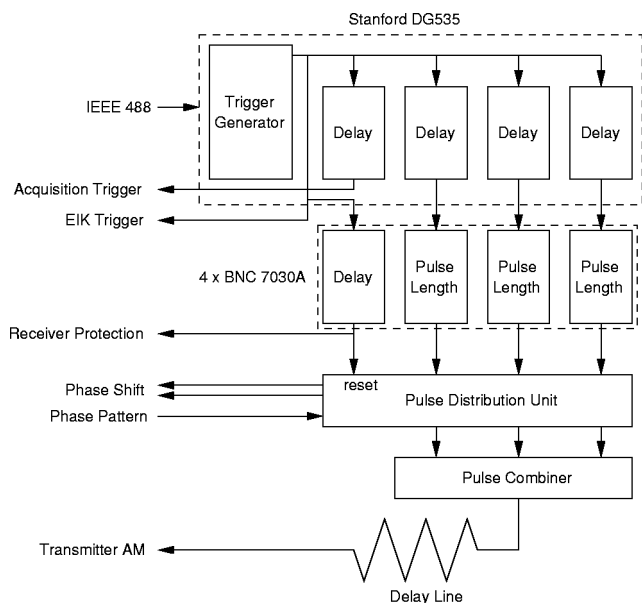


FIG. 7. Block diagram of the timing system. Two stages of delay generators are used to define pulse delays and durations. A pulse distribution unit is used to gate individual pulses and control the transmitter phase shifters on a per pulse basis.

separate pulse channels to facilitate sequences with different numbers of pulses under computer control. In addition, the PDU provides two additional digital outputs which are sequenced according to a programmed pattern at the occurrence of each input pulse. These signals are used to control the phase shifters of the 95 GHz transmitter for each pulse. The gating of individual channels and the phase sequence are programmed by the main acquisition computer using a dedicated parallel interface that allows fast updates ( $<100 \mu\text{s}$ ).

A coaxial line delays the signal used to key the 95 GHz transmitter by  $\approx 60 \text{ ns}$  in order to compensate for switching delays and settling time of the phase shifters.

The electron beam of the EIK amplifier tube is enabled for a fixed  $1 \mu\text{s}$  period at the start of the pulse sequence. This currently limits the length of the sequence to  $1 \mu\text{s}$ . An additional delay generator (Berkeley Nucleonics 7030A), triggered at the start of the pulse sequence, enables the receiver after the pulse sequence is complete. Due to the fixed on-time of the amplifier tube, the repetition rate is limited by duty cycle considerations to about 10 kHz. These shortcomings will be addressed in the near future (see Sec. IV).

### 3. Digitizer

The sample response to the excitation mm-wave pulses is recorded using two peripheral component interconnect (PCI)-based fast averaging digitizers (Acqiris, Geneva, Switzerland, model AP100). The digitizers have an 8-bit resolution and a maximum sampling rate of 1 GS/s, thus spanning a frequency range of  $\pm 500 \text{ MHz}$  centered on the frequency of the excitation mm-wave signal. The digitized signal can be averaged in real time up to 24-bits depth before it has to be read out by the host computer. As a result, there is negligible dead time ( $<1 \mu\text{s}$ ) after each acquisition, and the effective repetition rate of the pulsed experiment is not unduly limited. The digitizers also offer a large record length and

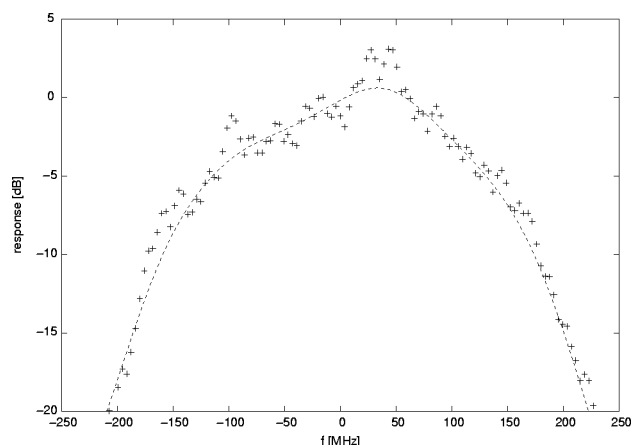


FIG. 8. Spectrometer frequency response as determined from the FID of lithium phthalocyanine at various magnetic fields  $B_0$ . The phthalocyanine powder was glued to a sample holder filled with water, imitating an aqueous sample. The estimated 3 dB bandwidth is 200 MHz.

may collect traces longer than  $100 \mu\text{s}$  without reducing the sample rate, avoiding the need to trade bandwidth for spectral resolution.

## III. EXPERIMENTAL CHARACTERIZATION

### A. Bandwidth

The effective bandwidth of the spectrometer is determined by two main factors: (i) The bandwidth of the spectrometer components, and (ii) the bandwidth of a mm-wave pulse to achieve a desired spin-flip angle (typically  $\pi/2$ ). With the exception of the EIK amplifier, which is operated in the saturated regime, the spectrometer components are linear, i.e., their frequency response is independent of the power level. In contrast, the duration  $t_p$ , and therefore the spectral bandwidth  $\Delta f_{\text{exc}}$ , of pulses for a given flip angle depends on the  $B_1$  field strength at the sample [Eq. (1)]. The relative significance of these factors depends therefore on the available mm-wave power.

The overall frequency response of the spectrometer components was determined by measuring the free induction decay (FID) of lithium phthalocyanine after a short ( $<4 \text{ ns}$ ) excitation pulse at various magnetic fields  $B_0$ , resulting in free induction decay signals of different frequency. The amplitude and the frequency of the FID were extracted from the time trace by a Fourier transform. To mimic a typical aqueous sample, the phthalocyanine was dispersed in a thin film of polystyrene on a sandwich of microscope glass cover slips separated by a  $25 \mu\text{m}$  thick layer of water. The measured frequency response is shown in Fig. 8. The  $-3 \text{ dB}$  bandwidth is on the order of 200 MHz, which is comparable to that achieved at  $Ku$ -band frequencies.<sup>21</sup> The observed response is not a simple Lorentzian, indicating that other components beside the resonator play a significant role. A small amount of ripple is noticeable in the frequency response data; this is likely due to parasitic resonances caused by minor reflections in the overall signal path (see also Sec. III B). The steep slopes beyond  $\Delta f \approx \pm 150 \text{ MHz}$  are attributed to the limited bandwidth of the excitation mm-wave pulse.

An ideal fast-switched mm-wave pulse of duration  $t_p$  has a spectral power distribution of

$$p(f_0 + \Delta f) \propto \frac{\sin^2(2\pi t_p \Delta f)}{(2\pi t_p \Delta f)^2}. \quad (4)$$

We typically achieve  $\pi/2$  pulse durations of  $t \approx 4$  to 6 ns. In practice, the spectral coverage is more uniform than suggested by Eq. (4), and we generally observe  $-3$  dB bandwidths of  $>150$  MHz. We attribute this to the nonlinear kinetics of the transverse magnetization<sup>20</sup> as well as phase modulation effects during pulse transients, caused by the pulse forming  $p$ - $i$ - $n$  diode switches and/or compression effects in the EIK amplifier tube as the saturated regime is reached. This phase distortion may be thought of as a beneficial form of frequency “chirp” that helps to spread out the power density more evenly in the frequency domain.<sup>35</sup>

## B. Dead time

Short dead times are critical for measuring FIDs with short decay times. In pulsed spectrometers at lower frequencies, the dead time is typically dominated by the ringing of the resonator after the last pulse

$$r_Q(t) \propto e^{-2\pi f_0 t/Q}, \quad (5)$$

where  $Q$  is the quality factor of the resonator and  $f_0$  is the resonant frequency. In high-frequency spectrometers, ringing of the resonator decays faster, and other contributions to the dead time therefore gain in relative importance.<sup>5</sup>

In our spectrometer, one dominant contribution appears to be standing waves in the corrugated waveguide section connecting the resonator with the duplexer unit. Assuming that a slight mismatch at both waveguide ends gives rise to power reflection coefficients  $R_1$  and  $R_2$ , a mm-wave pulse being reflected back and forth will be attenuated by a factor of  $R_1 \times R_2$  on each round trip.<sup>21</sup> The round trip time is

$$t_{\pi} = \frac{2\ell}{c}, \quad (6)$$

where  $\ell$  is the waveguide length and  $c$  is the group velocity which is here essentially the same as for free-space propagation. The amplitude of the ringing signal,  $r_{wg}$  decays therefore according to

$$r_{wg}(t) \propto \sqrt{(R_1 R_2)^{t/t_{\pi}}} = (R_1 R_2)^{ct/4\ell}. \quad (7)$$

This term is independent of the frequency used, but depends exponentially on the length of the waveguide. Even at very low reflectivities, the quality factor  $Q$  of this parasitic highly overmoded resonator can be significant. In our case, the waveguide length is  $\ell = 900$  mm, corresponding to  $t_{\pi} = 6$  ns, which is comparable to typical pulsed spectrometers at lower frequencies. This corresponds to a “mode spacing” of 166 MHz, which likely is a contributing factor to the ripple in Fig. 8. To illustrate this effect, we assume the reflectivity at the waveguide/duplexer interface as  $R_1 = 1\%$ , whereas a reasonably matched resonator might have a reflectivity  $R_2 = 5\%$ . At an incident pulse power of 1 kW and a coupling between the orthogonally polarized modes of  $-20$  dB (caused by imperfect symmetry of the resonator), it

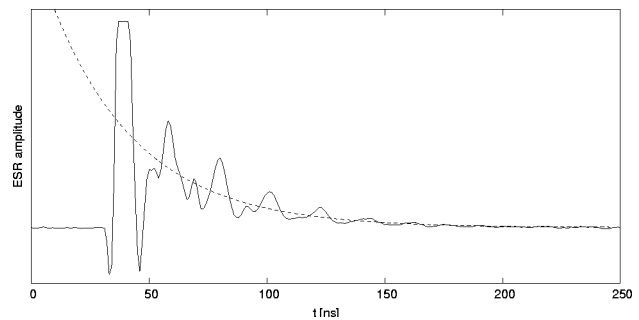


FIG. 9. 64-shot average of the free induction decay (solid) of 500 nl of 1 mM solution of 4-acetamido-TEMPO in water at room temperature, illustrating dead time and sensitivity.  $t=0$  marks the end of the exciting 5 ns pulse. At  $t=30$  ns, the receiver protection is turned off. The signal emerges at  $t \approx 45$  ns from artifacts due to ringdown and receiver overload. The dashed curve is a fit of the resonant component of the FID, used to determine the SNR.

would take  $\approx 20$  ns for the ringing to decay down to 1 nW in the detection arm. Note that this corresponds to a parasitic  $Q \approx 1000$ , considerably larger than that of the resonator itself. The waveguide length  $\ell$  cannot be significantly reduced due to geometrical constraints of the magnet system used. Compensating for this by reducing the already very small reflections at the waveguide ends is difficult, especially as for a given time  $t$ , the ringing amplitude scales as a power law with respect to the reflectivities, compared to an exponential dependence on the waveguide length.

Another factor contributing to the dead time is the noise tail of the EIK power amplifier. The process of turning off the EIK after the last pulse takes on the order of 10 ns. In addition, there is some timing jitter with respect to the last transmitted pulse, which presently requires us to leave the EIK enabled for another 10 ns after the last pulse.

With the current setup, we consistently achieve dead times of  $t_d \leq 50$  ns (see Fig. 9, for an example). If the ESR signal is sufficiently strong, it is practical to introduce attenuation in the received signal path in order to bring the signal back into the dynamic range of the receiver. Under these favorable conditions, we have achieved dead times as low as  $t_d \approx 30$  ns.

## C. Sensitivity

The sensitivity of the spectrometer for an aqueous sample was experimentally determined by measuring the FID of 1 mM 4-acetamido-TEMPO in water at room temperature. At an effective sample volume of 500 nl, this corresponds to  $N = 3 \times 10^{14}$  spins. The corresponding signal, averaged  $n = 64$  times, is shown in Fig. 9. One of the three hyperfine-split ESR transitions is resonant and leads to an exponentially decaying FID; the other two transitions show up as oscillatory signals. By fitting an exponential decay curve to the FID signal (thereby ignoring the oscillating signal contributions of off-resonant transitions) and determining the cumulative root-mean-square amplitude of the full-bandwidth noise tail after the FID for both quadrature channels, a signal-to-noise ratio (SNR) (back extrapolated to zero dead time) of  $\approx 550$  was obtained. When the noise bandwidth

is limited to the useful bandwidth of the spectrometer ( $\Delta f = 200$  MHz),<sup>36</sup> we obtain  $\text{SNR} \approx 730$ .

Defining the sensitivity as the number of spins required to achieve a SNR of 1:1, we arrive at a threshold of

$$N_{\text{single}} = \frac{N\sqrt{n}}{3\text{SNR}} = 1.1 \times 10^{12}, \quad (8)$$

for a single-shot experiment (where the factor 1/3 corrects for the intensity of the neglected nonresonant hyperfine-split transitions). Given a repetition rate of  $f_{\text{rep}} = 10$  kHz, the sensitivity as a function of acquisition time is given as

$$N(t) = N_t / \sqrt{t}, \quad (9)$$

where

$$N_t = \frac{N_{\text{single}}}{\sqrt{f_{\text{rep}}}} = 1.1 \times 10^{10} \sqrt{s}. \quad (10)$$

It should be noted that, at room temperature, the thermal polarization is only about  $8 \times 10^{-3}$ , and the effective number of spins is greatly decreased. Assuming that the noise level is essentially independent of the sample temperature, the sensitivity would then scale with temperature as

$$N_{\text{single}}(T) = \frac{8.3 \times 10^9}{h\nu} \frac{1}{\tanh \frac{2kT}{h\nu}}, \quad (11)$$

and, as far as relaxation times allow the repetition rate to be maintained,

$$N_t(T) = \frac{8.3 \times 10^7}{h\nu} \sqrt{s} \frac{1}{\tanh \frac{2kT}{h\nu}}. \quad (12)$$

The above numbers are based on the back-extrapolated initial SNR, i.e., neglecting signal decay. The dead time of the spectrometer increases the required number of spins by

$$N \propto e^{t_d(1/T_2 + 1/T_2^*)}, \quad (13)$$

in an FID experiment (where for simplicity we have taken the inhomogeneous broadening  $T_2^*$  to be Lorentzian), or about a factor of 3 for the example shown in Fig. 9. The corresponding factor in a spin-echo experiment is

$$N \propto e^{2t_d/T_2}. \quad (14)$$

Furthermore, in a real experiment, the decaying signal is acquired for a finite record length  $t_{\text{max}}$ . Accumulating the decaying signal (and the constant noise background) over a record length of five time constants [ $t_{\text{max}} = 5(T_2 T_2^*) / (T_2 + T_2^*)$ ],<sup>37</sup> the sensitivity is reduced by a factor of 2.5.<sup>21</sup>

Sensitivity assessments for pulsed ESR spectrometers in the literature are somewhat scarce and usually not directly comparable. For a  $Ku$ -band (17 GHz) spectrometer, a sensitivity of  $N_t = 6 \times 10^{13} \sqrt{s}$  spins was given<sup>21</sup> at similar shot repetition rates, but for the 2D-ELDOR experiment.

For a narrow-band ( $\Delta f' = 30$  MHz) pulsed  $W$ -band (94.9 GHz) spectrometer using a  $Q' = 3000$  resonator, a room-temperature single-shot FID sensitivity was estimated.<sup>3</sup> In comparing our sensitivity to this value, the bandwidth and

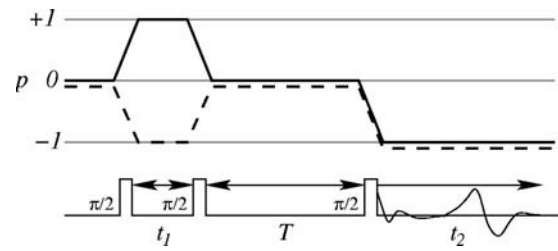


FIG. 10. 2D-ELDOR pulse sequence and coherence pathways for the  $S_{c+}$  (dashed) and  $S_{c-}$  (solid) signals.  $t_1$  is stepped out and the signal is recorded along the  $t_2$  axis. The data set is then Fourier transformed to obtain the 2D spectrum. Several other coherence paths generating contributions to the acquired signal are eliminated by phase cycling and have been omitted from this figure for clarity.

resonator  $Q$  have to be taken into account. Assuming uniform spectral noise density and considering that the power extracted from the induction signal is proportional to  $Q$ , we obtain an “equivalent sensitivity” of

$$N'_{\text{single}} = N_{\text{single}} \sqrt{\frac{\Delta f' Q}{\Delta f Q'}}, \quad (15)$$

$$N'_{\text{single}} = 1.3 \times 10^{11}. \quad (16)$$

This compares favorably with the value of  $3.1 \times 10^{11}$  spins reported earlier.<sup>3</sup>

#### D. Example: Two-dimensional electron-electron double resonance spectroscopy

2D-ELDOR<sup>16,37</sup> is an exchange correlation spectroscopy method closely related to that of NMR.<sup>38</sup> It is based on a sequence of three  $\pi/2$  pulses (Fig. 10). The first two pulses are used to produce  $p=0$  coherence (longitudinal magnetization) which is modulated during  $t_1$ , depending on the resonance frequency of the respective spin packet. During the mixing time  $T$ , polarization/coherence may be transferred between manifolds with different resonance frequencies. A final  $\pi/2$  pulse converts the  $p=0$  coherence to transverse magnetization which is then measured as a function of time  $t_2$ . By stepping out  $t_1$ , a 2D signal is collected. After Fourier transformation in  $t_1$  and  $t_2$ , the 2D spectrum effectively represents the exchange in the spin system during the mixing period  $T$ . Cross peaks, i.e., spectral intensity for  $f_1 \neq f_2$ , therefore mark transitions between states with resonant frequencies  $f_1$  and  $f_2$ .

There are two possible pathways to create the desired frequency dependent  $p=0$  coherence after the first two pulses. We refer to the associated coherence paths as  $S_{c+}$  or FID-like ( $p=0 \rightarrow -1 \rightarrow 0 \rightarrow -1$ ) and  $S_{c-}$  or spin echo-like ( $p=0 \rightarrow +1 \rightarrow 0 \rightarrow -1$ ). These contributions can be separated, and other undesired coherence paths can be suppressed by phase cycling techniques. The full 64-step phase cycle is automatically implemented by the spectrometer. It is a simple extension of the 32-step phase cycle commonly used in this experiment at lower frequencies.<sup>17,18,39</sup> While both  $S_{c+}$  and  $S_{c-}$  reflect the dynamics during the mixing period, significantly better resolution is obtained in the  $S_{c-}$  signal. This is because the  $S_{c-}$  signal is spin echo-like, i.e., inhomogeneous line broadening during the  $p=+1$  period gets

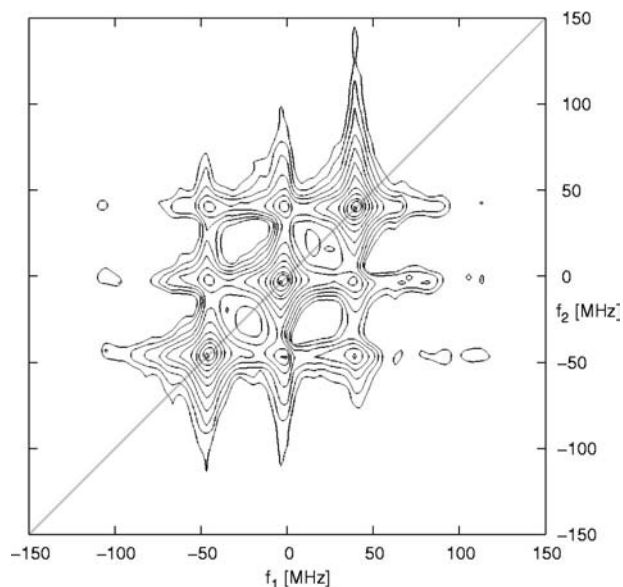


FIG. 11. Contour plot of the  $|S_{c-}|$  spectrum of TEMPO in decane at room temperature. The mixing time was  $T=100$  ns. Each contour represents a change of  $\sqrt{2}$  in amplitude.

partially cancelled during the  $p=-1$  period. Taking advantage of the enhanced resolution, we will consider only the  $S_{c-}$  signal in our examples.

In Fig. 11, we show a simple 2D-ELDOR experiment performed at 95 GHz. It illustrates the auto- and cross peaks that form during the mixing period  $T$ . It is a contour plot of the  $S_{c-}$  signal obtained from an  $\approx 2$  mM solution of 4-acetamido-TEMPO in *n*-decane at room temperature. Since this solvent has a low dielectric loss, a rather thick ( $\approx 150$   $\mu\text{m}$ ) sample could be employed, corresponding to an effective sample volume of 3  $\mu\text{l}$ . A reasonable, but not rigorous, effort was made to deoxygenate the sample. The experiment was performed for several mixing times  $T$ , ranging from 50 to 500 ns. Figure 11 corresponds to  $T=100$  ns. The time  $t_1$  was varied in 64 4 ns steps, while the induction signal was recorded with a  $t_2$  resolution of 1 ns. The duration of the  $\pi/2$  mm-wave pulses was 4 ns. The induction signal was averaged 16 times for each of the 64 steps in the phase cycle. The total number of recorded events is therefore  $64 \times 64 \times 16 = 65\,536$  events per 2D spectrum at a repetition rate of 5 kHz. The wall-clock acquisition time per spectrum was 24 s.

One may observe the contours of the three autopeaks ( $f_1=f_2$ ) along the positive diagonal. There are six cross-peaks ( $f_1 \neq f_2$ ) clearly visible in Fig. 11 forming a tic-tac-toe pattern. This is the characteristic 2D-ELDOR pattern that arises when Heisenberg spin exchange collisions are the dominant exchange mechanism.<sup>16</sup> This is to be expected in the low viscosity decane solvent, where collisions between TEMPO molecules are frequent, and the development of these crosspeaks with  $T$  may be analyzed to provide the exchange rate (cf. Sec. III E). The longitudinal relaxation time,  $T_1$  is readily obtained from the total intensity,  $I$  of the 2D-ELDOR signal versus mixing time,  $T$ .<sup>16,40</sup> (Here,  $I$  is obtained by integrating the whole 2D spectrum over  $f_1$  and  $f_2$ .) Using seven mixing times, we obtain  $T_1=(97 \pm 6)$  ns,

which is significantly shorter than  $T_1$  values typically obtained for similar nitroxides in solution at lower frequencies.<sup>40–42</sup> Thus, the overall decay of the 2D-ELDOR spectra with mixing time over the range of 50 to 500 ns is considerable, but the excellent SNR leads to good spectra, albeit with some increase in signal averaging needed for the longer mixing times.

### E. Example: Two-dimensional electron-electron double resonance in aqueous solution

Figures 12 and 13 show stack plots of the 2D-ELDOR  $S_{c-}$  signal of 1 mM TEMPO solutions in two water/glycerol mixtures of different composition at room temperature. Again, a reasonable effort was made to remove dissolved oxygen from the samples. This system serves as a model for biological samples, e.g., solutions of spin labeled proteins or membranes with high water content. Since these aqueous samples are much lossier than the decane sample, it was necessary to use a much thinner ( $\approx 25$   $\mu\text{m}$ ) sample, yielding an effective sample volume of only 0.5  $\mu\text{l}$ . Mixing times of  $T=50, 100, 250,$  and 500 ns (not shown) were chosen to sample the dynamics of the system. Again,  $t_1$  was varied in 64 4 ns steps while the induction signal was recorded with a  $t_2$  resolution of 1 ns. The duration of the  $\pi/2$  mm-wave pulses was 5 ns. Given the smaller sample size and lower concentration, the induction signal was averaged 1024 times for each of the 64 steps in the phase cycle. Thus, the total number of recorded events is  $64 \times 64 \times 1024 = 4\,194\,304$ , corresponding to 14 min of wall-clock acquisition time per 2D spectrum, again using a repetition rate of 5 kHz. One observes that a very good SNR is obtained despite the lossy samples of small size. We also observe much weaker crosspeaks than from decane (Fig. 11), which is qualitatively explained as a reduced rate of Heisenberg spin exchange collisions in the more viscous solvents.

A quantitative analysis of these 2D-ELDOR spectra can be obtained by means of spectral simulation and fitting packages.<sup>43</sup> The dynamic parameters obtained from the spectra in Figs. 12 and 13 are shown in Table II. In these viscous solvents wherein rotational (and translational) diffusion is slowed down, incomplete rotational averaging of the hyperfine and  $g$  tensors becomes an important spin relaxation mechanism. It leads to the observed variation in amplitudes of the autopeaks, and also contributes to the development of crosspeaks. The analysis provides the rotational diffusion constant  $R$ , as well as the Heisenberg exchange rate,  $\Delta_{\text{HE}}$ . The more viscous 40% (by volume) glycerol–water solution exhibits broader lines and greater width and amplitude variation of the autopeaks. The obtained rotational diffusion rates for both samples differ by a factor of  $\approx 2.5$ . This agrees with the change of viscosity ( $\eta_{10\%} = 1.153 \times 10^{-3}$  Pa s versus  $\eta_{40\%} = 3.181 \times 10^{-3}$  Pa s at room temperature),<sup>45</sup> assuming the validity of the Stokes–Einstein–Debye relation for this rapidly tumbling system. The Heisenberg exchange is also observed to decrease with the increased viscosity. The analysis also distinguishes between other sources of  $T_2$  relaxation (given as residual  $T_2$  in Table II), such as spin rotational relaxation,<sup>41</sup> which yields additional homogeneous broaden-

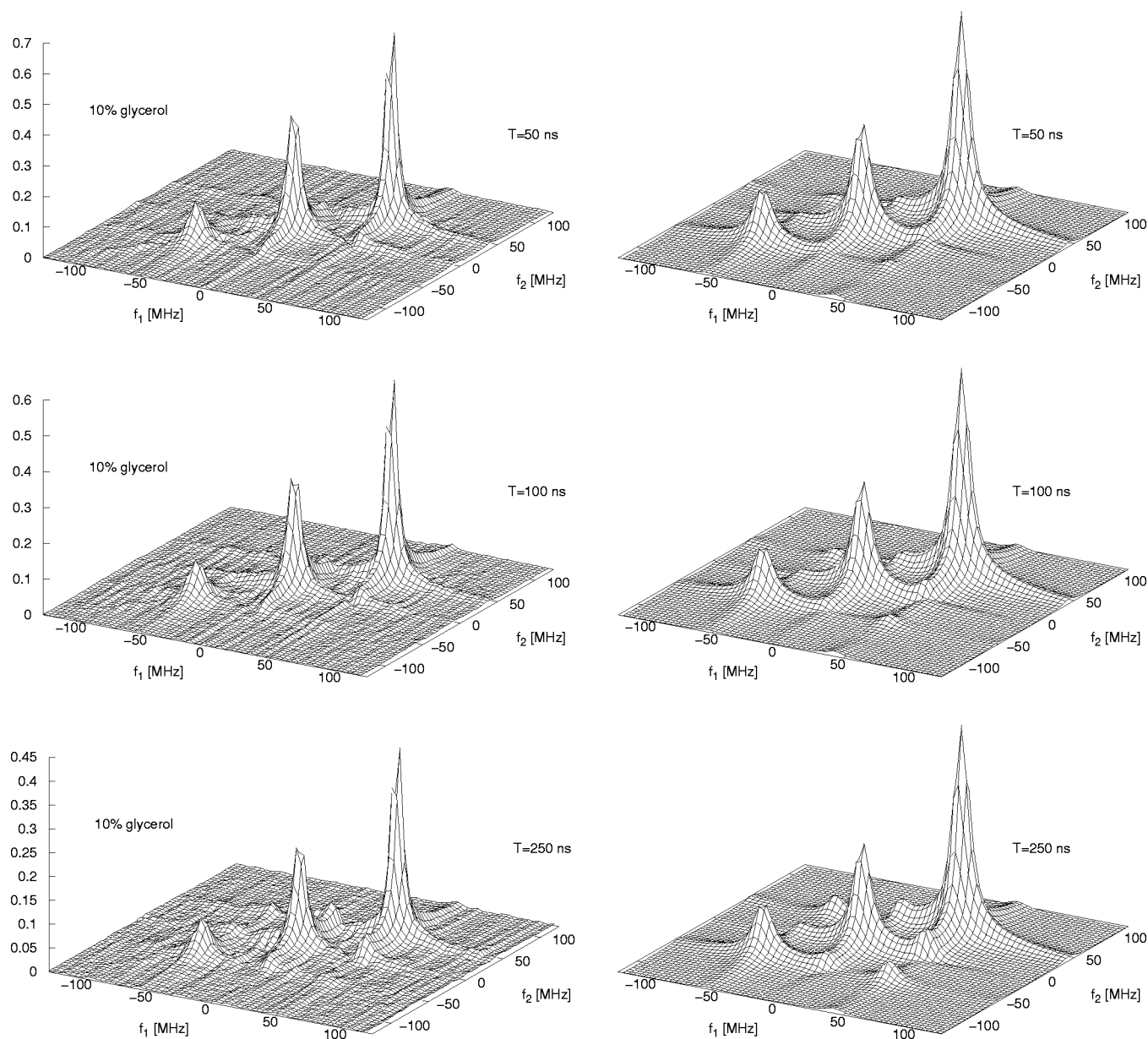


FIG. 12. Experimental (left-hand side) and simulated (right-hand side) 2D-ELDOR  $S_{c-}$  spectra of 1 mM 4-acetamido-TEMPO solution in 90% water/10% glycerol at room temperature for various mixing times  $T$ .

ing, from the inhomogeneous (assumed) Gaussian broadening, such as from unresolved proton hyperfine couplings. Also the  $T_1$  relaxation times are observed to decrease as the glycerol content increases. These short  $T_1$  and residual  $T_2$  values at 95 GHz suggest the possibility of a field or frequency dependent spin relaxation mechanism that is ineffective at lower fields and frequencies. One such mechanism could be dynamic modulation of the  $g$  value due to rapid solvent-induced fluctuations,<sup>46,47</sup> but more detailed studies are required.

#### IV. DISCUSSION

We have shown that an effective high-power high-bandwidth pulsed 95 GHz ESR spectrometer can be built using commercially available components and parts easily made in a machine shop. The quasi-optical bridge and the

Fabry-Pérot resonator with its coupling mesh have been found to provide the low-loss and excellent polarization purity required for the induction-mode experiment that provides the needed isolation ( $>20$  dB) between the excitation mm-wave pulses and the detector.

The spectrometer is suitable for aqueous samples at physiological temperatures and, therefore, for investigations of molecular and spin dynamics in biological samples which are either not viable or of limited interest in frozen solution at low temperatures. The reported experiments on nitroxide radicals provide examples to demonstrate the capabilities of the instrument and the value of 2D-ELDOR experiments. They also demonstrate the significantly enhanced sensitivity per spin compared to high-power pulsed ESR and ELDOR at lower frequencies.

More complex samples include spin labels dispersed in biological or biomimetic membranes. For large, nonspherical

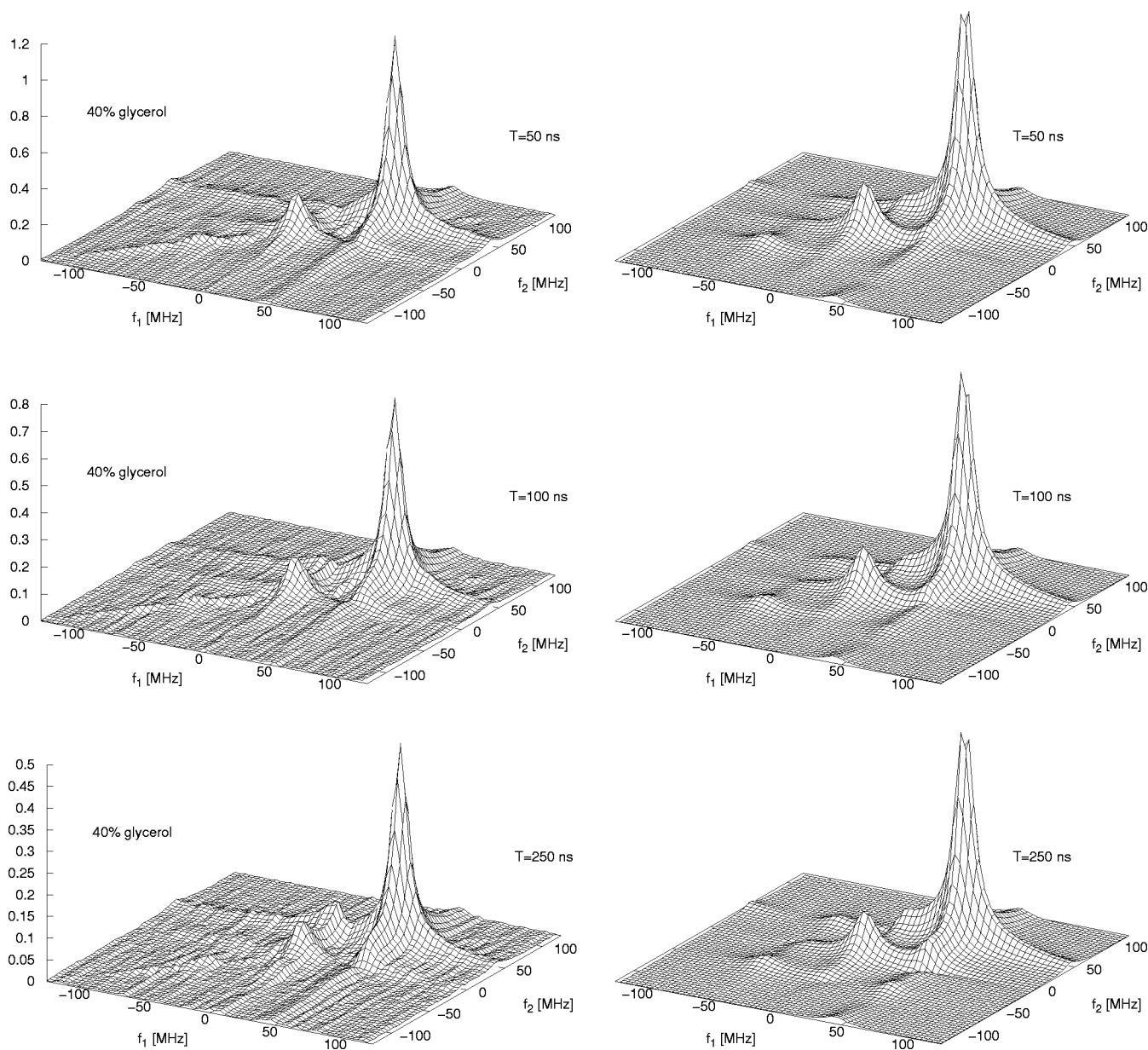


FIG. 13. Experimental (left-hand side) and simulated (right-hand side) 2D-ELDOR  $S_{c-}$  spectra of 1 mM 4-acetamido-TEMPO solution in 60% water/40% glycerol at room temperature for various mixing times  $T$ .

spin labels, the rotational diffusion may be anisotropic, and the labels can experience an ordering potential in the liquid-crystalline or liquid-ordered matrix, giving rise to a wealth of parameters that can be assessed using 2D-ELDOR and similar experiments.<sup>17,18,40,48</sup> In a similar fashion, site-directed spin labeling of proteins<sup>49</sup> can be used to probe the molecular dynamics in proteins as already demonstrated for polypeptides.<sup>50</sup> While the spectral coverage we have achieved so far may not be sufficient to obtain the full spectrum of slowly tumbling spin labels in these systems ( $\approx 500$  MHz at 95 GHz), it should still be possible to infer detailed information from partial spectra of regions particularly sensitive to the molecular dynamics. In addition, with field-stepping ESR methods<sup>16,51</sup> which we are planning to implement, it would still be possible to experimentally query different spectral regions in correlation experiments. Again,

we comment that the full value of 95 GHz experiments will be realized in multifrequency studies.

Furthermore, time resolved and Fourier transform HFESR have a significant potential for studying both the kinetics and the electronic and geometric structure of intermediate states in electron transfer processes, e.g., in photosynthetic reaction centers.<sup>52</sup> Due to the small  $g$  anisotropy of most involved organic radicals, the enhanced Zeeman resolution of HFESR is highly beneficial in this application. Since the spectrometer supports physiological conditions, i.e., liquid aqueous samples, such experiments could in principle be performed on live cells.

The current timing system has several shortcomings that limit the complexity and sensitivity of possible experiments. At present, up to three mm-wave pulses occurring within a fixed time window during which the EIK is enabled are pos-

TABLE II. Dynamic spin system parameters extracted from the 2D-ELDOR spectra of 4-acetamino-TEMPO in water/glycerol solution at room temperature. An isotropic rotational diffusion rate  $R$  is assumed.  $\Delta_{\text{HE}}$  and  $\Delta_{\text{G}}$  are the Heisenberg exchange rate and the Gaussian inhomogeneous linewidth, respectively. The principal  $g$  values ( $g_{xx}=2.00878$ ,  $g_{yy}=2.00604$ ,  $g_{zz}=2.00215$ ) and hyperfine couplings ( $A_{xx}=0.62$  mT,  $A_{yy}=0.77$  mT,  $A_{zz}=3.74$  mT) used in the analysis are estimates based on a similar sample.<sup>a</sup> The longitudinal relaxation time  $T_1$  was estimated from the integrated intensities of the 2D spectra.

Parameter	10% glycerol	40% glycerol	Unit
$R$	6.31	2.51	$10^9 \text{ s}^{-1}$
$\Delta_{\text{HE}}$	1.86	1.26	$10^6 \text{ s}^{-1}$
$\Delta_{\text{G}}$	0.1	0.1	mT
$T_1$	290	96	ns
Residual $T_2$	68	71	ns

<sup>a</sup>See Ref. 44.

sible. We plan to implement a new timing subunit that will eliminate these shortcomings, allowing for more complex pulse sequences and providing more detailed control over individual control signals. These improvements are also expected to reduce jitter of the EIK shut-off signal, thereby improving the dead time. By enabling the EIK amplifier on a per pulse basis, much higher repetition rates will become possible without exceeding the permissible duty cycle, thereby reducing acquisition time and effectively increasing the sensitivity of the spectrometer [Eq. (10)]. Possible negative effects of the amplifier dark noise between the pulses would also be avoided.

Finally, we note the quasioptical spectrometer technology that we have developed at 95 GHz should be extendable (with appropriate high-power amplifiers) to higher frequencies, where it is required even more.

## ACKNOWLEDGMENTS

The authors would like to thank P. Borbat for his assistance with the phase cycling hardware and the transceiver specifications, and Z. Liang for performing the spectral simulations. The donation of a 6 T NMR magnet by Professor R. M. Cotts and Professor D. F. Holcomb (Physics Department, Cornell University) is greatly appreciated. The authors would also like to thank the Physics Department of Cornell University for access to the graduate machine shop and Nate Ellis of the LASSP shop for machining the off-axis elliptical mirrors. Seth Marks of Protolab Engineering machined many parts used in the initial development phase of the spectrometer. This work was funded by an NIH/NCRR grant and by the NSF.

<sup>1</sup>O. Y. Grinberg, A. A. Dubinskij, and Y. S. Lebedev, *Russ. Chem. Rev.* **52**, 850 (1983).

<sup>2</sup>W. B. Lynch, K. A. Earle, and J. H. Freed, *Rev. Sci. Instrum.* **59**, 1345 (1988).

<sup>3</sup>J. Allgeier, J. A. J. M. Disselhorst, R. T. Weber, W. T. Wenckebach, and J. Schmidt, in *Modern Pulsed and Continuous-Wave Electron Spin Resonance*, edited by L. Kevan and M. K. Bowman (Wiley, New York, 1990), Chap. 6.

<sup>4</sup>K. A. Earle, D. S. Tipikin, and J. H. Freed, *Rev. Sci. Instrum.* **67**, 2502 (1996).

<sup>5</sup>T. Prisner, S. Un, and R. G. Griffin, *Isr. J. Chem.* **32**, 357 (1992).

<sup>6</sup>T. Prisner, M. Rohrer, and K. Möbius, *Appl. Magn. Reson.* **7**, 167 (1994).

<sup>7</sup>G. M. Smith, J. C. G. Lesurf, R. H. Mitchell, and P. C. Riedi, *Rev. Sci. Instrum.* **69**, 3924 (1998).

<sup>8</sup>I. Gromov, V. Krymov, P. Manikandan, D. Arieli, and D. Goldfarb, *J. Magn. Reson.* **139**, 8 (1999).

<sup>9</sup>D. Schmalbein, G. G. Maresch, A. Kamlowski, and P. Höfer, *Appl. Magn. Reson.* **16**, 185 (1999).

<sup>10</sup>M. R. Fuchs, T. F. Prisner, and K. Möbius, *Rev. Sci. Instrum.* **70**, 3681 (1999).

<sup>11</sup>M. J. Nilges, A. I. Smirnov, R. B. Clarkson, and R. L. Belford, *Appl. Magn. Reson.* **16**, 167 (1999).

<sup>12</sup>D. E. Budil, K. A. Earle, W. B. Lynch, and J. H. Freed, in *Advanced EPR: Applications in Biology and Biochemistry*, edited by A. J. Hoff (Elsevier, Amsterdam, Netherlands, 1989), Chap. 8.

<sup>13</sup>G. R. Eaton and S. S. Eaton, *Appl. Magn. Reson.* **16**, 161 (1999).

<sup>14</sup>J. H. Freed, *Annu. Rev. Phys. Chem.* **51**, 655 (2000).

<sup>15</sup>P. P. Borbat, A. J. Costa-Filho, K. A. Earle, J. K. Moscicki, and J. H. Freed, *Science* **291**, 266 (2001).

<sup>16</sup>J. Gorcester, G. L. Millhauser, and J. H. Freed, in *Modern Pulsed and Continuous-Wave Electron Spin Resonance*, edited by L. Kevan and M. K. Bowman (Wiley, New York, 1990), Chap. 3.

<sup>17</sup>A. J. Costa-Filho, Y. Shimoyama, and J. H. Freed, *Biophys. J.* **84**, 2619 (2003).

<sup>18</sup>A. J. Costa-Filho, R. H. Crepeau, P. P. Borbat, M. T. Ge, and J. H. Freed, *Biophys. J.* **84**, 3364 (2003).

<sup>19</sup>J. H. Freed, in *Very High Frequency ESR*, *Biol. Magn. Reson.* Vol. 22, edited by O. Grinberg and L. J. Berliner (Kluwer, New York, 2004), Chap. 2.

<sup>20</sup>J. P. Hornak and J. H. Freed, *J. Magn. Reson.* **67**, 501 (1986).

<sup>21</sup>P. P. Borbat, R. H. Crepeau, and J. H. Freed, *J. Magn. Reson.* **127**, 155 (1997).

<sup>22</sup>*Introduction to Millimeter Extended Interaction Klystrons*, Communications and Power Industries Inc., 45 River Drive, Georgetown, ONL7G 224, Canada.

<sup>23</sup>P. F. Goldsmith, *Quasioptical Systems* (IEEE Press, Piscataway, NJ, 1998), Chap. 7.6.

<sup>24</sup>P. F. Goldsmith, *Quasioptical Systems* (IEEE, Piscataway, NJ, 1998), Chap. 8.3.

<sup>25</sup>J. L. Doan, in *Infrared and Millimeter Waves*, edited by K. J. Button (Academic, New York, 1985), Vol. 13, Chap. 4.

<sup>26</sup>A. G. van Nie, *Philips Res. Rep.* **19**, 378 (1964).

<sup>27</sup>P. F. Goldsmith, *Quasioptical Systems* (IEEE, Piscataway, NJ, 1998), Chap. 9.9.

<sup>28</sup>J. P. Barnes and J. H. Freed, *Rev. Sci. Instrum.* **69**, 3022 (1998).

<sup>29</sup>P. F. Goldsmith, *Quasioptical Systems* (IEEE, Piscataway, NJ, 1998), Chap. 9.2.

<sup>30</sup>We thank Millitech Corp., Northampton, MA for the gift of several meshes that were used in early stages of this work.

<sup>31</sup>G. van Rossum and J. de Boer, *CWI Quarterly* **4**, 283 (1991).

<sup>32</sup>E. Anderson, Z. Bai, C. Bischof, S. Blackford, J. Demnel, J. Dongarra, J. DuCroz, A. Greenbaum, S. Hammarling, A. McKenney, and D. Sorensen, *LAPACK Users' Guide*, 3rd ed. (Society for Industrial and Applied Mathematics (SIAM), Philadelphia, PA).

<sup>33</sup><http://www.netlib.org/fftpack>.

<sup>34</sup>D. Crawford, GNUPLOT, an Interactive Plotting Program, 1998, available electronically from <http://gnuplot.sourceforge.net/docs/gnuplot.html>.

<sup>35</sup>J. M. Bohlen, I. Burghardt, M. Rey, and G. Bodenhausen, *J. Magn. Reson.* **90**, 183 (1990).

<sup>36</sup>Limiting the noise bandwidth is equivalent to cropping the Fourier transformed spectrum to the region of interest, and no explicit filtering is necessary.

<sup>37</sup>J. Gorcester and J. H. Freed, *J. Chem. Phys.* **85**, 5375 (1986).

<sup>38</sup>J. Jeener, B. H. Meier, P. Bachmann, and R. R. Ernst, *J. Chem. Phys.* **71**, 4546 (1979).

<sup>39</sup>R. H. Crepeau, S. Saxena, S. Lee, B. Patyal, and J. H. Freed, *Biophys. J.* **66**, 1489 (1994).

<sup>40</sup>V. S. Sastry, A. Polimeno, R. H. Crepeau, and J. H. Freed, *J. Chem. Phys.* **105**, 5753 (1996).

<sup>41</sup>J. S. Hwang, R. P. Mason, L.-P. Hwang, and J. H. Freed, *J. Phys. Chem.* **79**, 489 (1975).

<sup>42</sup>R. W. Quine, S. S. Eaton, and G. R. Eaton, *Rev. Sci. Instrum.* **63**, 4251 (1992).

<sup>43</sup>D. E. Budil, S. Lee, S. Saxena, and J. H. Freed, *J. Magn. Reson.* **120**, 155 (1996).

<sup>44</sup>M. A. Ondar, O. Y. Grinberg, A. A. Dubinskij, and Y. S. Lebedev, *Khim.*

- Fiz. **3**, 527 (1984).
- <sup>45</sup> *Handbook of Chemistry and Physics*, edited by C. D. Hodgman, R. C. Weast, and S. M. Selby (CCRC Press, Cleveland, OH, 1955), p. 2025.
- <sup>46</sup> J. Gendell, J. H. Freed, and G. K. Fraenkel, *J. Chem. Phys.* **37**, 2832 (1962).
- <sup>47</sup> K. A. Earle, J. K. Moscicki, M. Ge, and J. H. Freed, *Biophys. J.* **66**, 1213 (1994).
- <sup>48</sup> D. Xu, R. H. Crepeau, C. K. Ober, and J. H. Freed, *J. Phys. Chem.* **100**, 15873 (1996).
- <sup>49</sup> W. L. Hubbell, D. S. Cafiso, and C. Altenbach, *Nat. Struct. Biol.* **7**, 735 (2000).
- <sup>50</sup> S. Saxena and J. H. Freed, *J. Phys. Chem. A* **101**, 7998 (1997).
- <sup>51</sup> A. A. Dubinskij, Y. A. Grishin, A. N. Savitsky, and K. Möbius, *Appl. Magn. Reson.* **22**, 369 (2002).
- <sup>52</sup> S. G. Zech, W. Hofbauer, A. Kamlowski, P. Fromme, D. Stehlik, W. Lubitz, and R. Bittl, *J. Phys. Chem. B* **104**, 9728 (2000).